

Acquiring GNSS Signals in Cislunar Space: A Hardware-in-the-Loop Investigation for LuGRE Mission Data

Original

Acquiring GNSS Signals in Cislunar Space: A Hardware-in-the-Loop Investigation for LuGRE Mission Data / Sciacca, Lorenzo; Minetto, Alex; Nardin, Andrea; Tedesco, Simone; Boschiero, Matilde; Fantinato, Samuele; Canzian, Luca; Dovis, Fabio. - ELETTRONICO. - (2025), pp. 1036-1045. (2025 IEEE/ION Position, Location and Navigation Symposium (PLANS) Salt Lake City (USA) April 28 - May 1, 2025) [10.1109/plans61210.2025.11028293].

Availability:

This version is available at: 11583/3001148 since: 2025-06-20T07:59:53Z

Publisher:

IEEE

Published

DOI:10.1109/plans61210.2025.11028293

Terms of use:

This article is made available under terms and conditions as specified in the corresponding bibliographic description in the repository





Publisher copyright

IEEE postprint/Author's Accepted Manuscript

©2025 IEEE. Personal use of this material is permitted. Permission from IEEE must be obtained for all other uses, in any current or future media, including reprinting/republishing this material for advertising or promotional purposes, creating new collecting works, for resale or lists, or reuse of any copyrighted component of this work in other works.

(Article begins on next page)

Acquiring GNSS Signals in Cislunar Space: A Hardware-in-the-Loop Investigation for LuGRE Mission Data

Lorenzo Sciacca¹ , Alex Minetto¹ , Andrea Nardin¹ , Simone Tedesco², Matilde Boschiero²,
Samuele Fantinato², Luca Canzian², Fabio Dovis¹ 

¹Politecnico di Torino, Turin, Italy

²Qascom s.r.l., Bassano del Grappa, Italy

Abstract—The use of Global Navigation Satellite System (GNSS) signals in cislunar space is gaining interest as a means to enhance navigation autonomy for lunar missions. This work investigates the acquisition of GNSS signals in this challenging environment, using a dataset obtained leveraging a hardware-in-the-loop experimental setup including the QN400-SPACE GNSS receiver and a Radio Frequency Constellation Simulator (RFCS). The study focuses on the processing of short batches of signals in the low-fidelity operating mode, characterized by a constrained sampling frequency and quantization levels. To enhance acquisition sensitivity, we explore various techniques, including Doppler compensation on the spreading code and exhaustive bit search strategies. Experimental results demonstrate the impact of Doppler correction on improving correlation peak sharpness and increasing successful acquisitions. This work establishes a baseline for testing high-sensitivity acquisition techniques on actual mission data once they are publicly released to the GNSS community, contributing to the advancement of GNSS-based navigation solutions for future lunar and deep-space exploration missions.

Index Terms—Global Navigation Satellite System (GNSS), Hardware-in-the-Loop (HIL), Correlators, Digital signal processing.

I. INTRODUCTION

To expand navigation capabilities beyond Earth’s orbit and support future lunar missions, it is crucial to research how GNSS signals are received in cislunar space. Reliable GNSS signal reception in this region can significantly enhance the autonomy of spacecraft by reducing reliance on ground-based systems and enabling critical operations like orbit determination, landing, and surface exploration. Therefore, understanding the challenges affecting GNSS performance in cislunar space is key to ensuring the success of upcoming lunar missions and exploring this new frontier effectively. As a collaborative effort between NASA, the Italian Space Agency (ASI), Qascom, and Politecnico di Torino’s NavSAS group, the LuGRE mission [1] offers a significant chance to evaluate the potential of GNSS for Position, Navigation, Timing (PNT) in the lunar and cislunar environments. Lunar GNSS Receiver Experiment (LuGRE), hosted aboard Firefly’s Blue Ghost Mission 1 (BGM1) currently en route to the Moon, provides essential observables, including pseudorange,

carrier phase, and Doppler measurements, as well as short batches of signal samples. These data are being transmitted from both lunar transfer orbit and the lunar surface to Earth. These batches, referred to as In-Phase/Quadrature samples (IQS) are subsequently analyzed to ascertain the availability and quality of GNSS signals and possible radio-frequency impairments acting in these extreme environments, providing valuable insights for future lunar missions.

Leveraging previous research [2]–[5], this paper examines the processing of short signal batches captured in the low-fidelity operational configuration of the LuGRE payload. The study is conducted in a controlled environment using a Spirent GSS7000 RFCS, which can emulate various mission scenarios at different distances from Earth, including lunar transfer orbit and operations on the lunar surface. The dataset under test is obtained by connecting the RFCS to the QN400-SPACE receiver [6]. The downlink transmission of these signal batches is limited by mission-specific limitations, which allows a limited set of configurations with sampling frequencies ranging from 4 MHz to 16 MHz and bit quantization levels of 4, 8, or 16 bits. This study focuses on the low-fidelity configuration, defined by a sampling frequency of 4 MHz and 4-bit quantization for L1, and 24 MHz 4-bit quantization for L5, which presents distinct challenges in signal processing due to its low-resolution nature. Despite these limitations, this configuration enables the generation of longer batches to be transmitted back to Earth in down-link. This study will focus also on evaluating acquisition parameters through post-processing acquisition using the techniques described in Section III. Conducted within a hardware-in-the-loop framework, this serves as a tuning process for the subsequent post-processing phase of the actual LuGRE IQS data.

The remainder of this paper is structured as follows: Section II provides background information on the characteristics of GNSS signals. Section III describes the methodology, detailing the acquisition techniques considered, and presents the hardware-in-the-loop simulation framework used to replicate mission scenarios at various distances from Earth. The experimental results are presented and discussed in Section IV, while Section V summarizes the main findings and highlights directions for future research based on actual LuGRE mission

data.

II. BACKGROUND

A. Signal model

GNSS rely on specialized signals transmitted from satellites to enable accurate and precise positioning and navigation. These signals, commonly referred to as Signal in Space (SIS), are transmitted in specific frequency bands across the electromagnetic spectrum. For instance, the upper L-band covers signals like GPS L1, Galileo E1, GLONASS G1, and BeiDou B1, whereas the lower L-band includes signals such as GPS L5, GLONASS G3, Galileo E5, and BeiDou B2. Fig. 1 shows the frequency allocation corresponding to Galileo E1/E5 and GPS L1/L5. To ensure efficient utilization of the

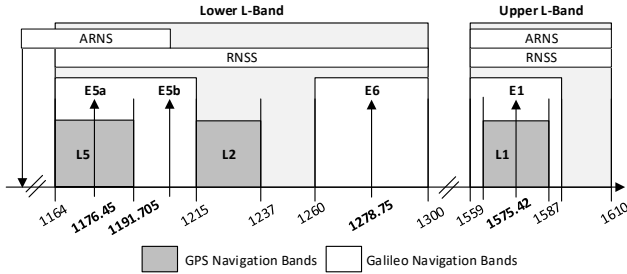


Fig. 1: Graphical representation of the GNSS frequency allocation. Source: European Space Agency (ESA).

shared spectrum among various constellations, GNSS signals employ a Code Division Multiple Access (CDMA) scheme. This approach allows multiple satellites to transmit over shared carriers while concurrently supporting diverse services.

A GNSS signal typically comprises three primary components:

- **Carrier signal:** This sinusoidal waveform is modulated according to a specific frequency, featuring in-phase and quadrature components. The carrier serves as the medium for transmitting the remaining signal components.
- **Ranging code(s):** These binary sequences, unique to each satellite, enable users to determine distances by accurately measuring the time delay of the received signal. Often referred to as Pseudo Random Noise (PRN) codes, they are crucial for accessing diverse positioning services.
- **Navigation data:** Carried by the radionavigation signal, this component provides critical information required for accurate positioning such as correction terms for measurements bias. It includes satellite orbital parameters (ephemeris), constellation-wide predictions (almanac), satellite clock corrections, and other parameters essential for mitigating timing errors.

Together, these components form the architecture of GNSS signals, enabling reliable and precise global positioning across a wide range of applications. The GNSS SIS can be characterized by various modulation schemes. A brief description of the modulations associated with the signals considered in this work is provided in Table I. A generic GNSS signal,

Signal	Modulation	Code rate [MHz]	Carrier frequency [MHz]	Data rate [Hz]	Secondary code length [PRN epochs]
GPS L1 C/A	BPSK(1)	1.023	1575.42	50	-
GPS L5 Q	BPSK(10)	10.23	1176.45	-	20
Galileo E1 OS-C	CBOC(6,1,1/11)	1.023	1575.42	-	25
Galileo E5a1	AltBOC(15,10)	10.23	1176.45	50	20

TABLE I: Main parameters characterizing the GNSS signals considered in this work.

transmitted by the i -th satellite, consisting of in-phase and quadrature components, can be expressed as:

$$x_{TX,i}(t) = A_I s_I(t) c_{i,I}(t) d_{i,I}(t) \cos(2\pi f_{C0} t + \theta_i) + A_Q s_Q(t) c_{i,Q}(t) d_{i,Q}(t) \sin(2\pi f_{C0} t + \theta_i) \quad (1)$$

where:

- A_I and A_Q represent the amplitudes of the in-phase and quadrature components, respectively.
- $s_I(t)$ and $s_Q(t)$: denote the in-phase and quadrature components of the subcarrier, respectively.
- $c_{i,I}(t)$ and $c_{i,Q}(t)$ represent the ranging/spreading codes associated with the i -th satellite for the in-phase and quadrature components, respectively.
- $d_{i,I}$ and $d_{i,Q}$ correspond to the navigation message data bits for the in-phase and quadrature components, respectively.
- θ_i denotes the phase of the carrier generated by the i -th satellite.
- f_{C0} is the carrier frequency.

Considering a receiver with a non-zero relative velocity $v(t)$ with respect to a given transmitting GNSS satellite, the carrier will experience a shift $f_D(t)$ given by the relationship:

$$f_D(t) = \frac{v(t)}{c} f_{C0} \quad (2)$$

Given the expression (1), and considering the Doppler effect on the whole signal, the expression of the in-phase component of the received signal can be written as:

$$r_{RX,I,i}(t) = \sqrt{2P_{I,RX}(t)} s_{i,I}(\omega(t)) c_{i,I}(\omega(t)) d_{i,I}(\omega_d(t)) \cos\left(2\pi f_{C0} \frac{t}{k_D(t)} + \theta_{i,RX}\right) + w_I(t) \quad (3)$$

where:

- $\omega(t) = -\tau + \frac{t}{k_D(t)}$, where τ is the code phase.
- $\omega_d(t) = -\tau_d + \frac{t}{k_D(t)}$, where τ_d is the propagation delay.
- $P_{I,RX}(t)$ is the received power of the in-phase component of the signal.
- $k_D(t) = 1 - \frac{f_D(t)}{f_{C0}}$.
- $f_D(t)$ is the value of the Doppler shift affecting the carrier.
- $w_I(t)$ represents the Additive White Gaussian Noise (AWGN) component of the in-phase signal.

A similar expression can be also obtained for the quadrature component.

III. METHODOLOGY

A. Acquisition techniques

Different techniques are present in literature to perform the evaluation of the Cross Ambiguity Function (CAF) with the aim of enhancing the receiver sensitivity [7] [8] [9] [10]. This section examines the application of consolidated coherent and non-coherent acquisition techniques, with a particular focus on addressing the impact of Doppler shift on the code and extending the coherent integration time for signals modulated by data bits. Initially, a brief review of standard coherent and non-coherent acquisition methods is presented to provide context. This is followed by the introduction of a technique to compensate for the effects of Doppler shift on the received spreading codes and a method for performing an exhaustive yet efficient bit search. The CAF is expressed as:

$$S(\bar{\tau}, \bar{f}_D) = |R(\bar{\tau}, \bar{f}_D)| = \left| \frac{1}{N} \sum_{n=0}^{N-1} y_{IF}[n] r_{IF}^*[n - \bar{\tau}] \right|^2 \quad (4)$$

where $r_{IF}[n]$ represents the locally generated code replica of length N at the intermediate frequency f_{IF} , defined as:

$$r_{IF}[n] = c[n] e^{j2\pi(f_{IF} + \bar{f}_D)n} \quad (5)$$

In this formulation, $y_{IF}[n]$ is the received signal, $c[n]$ is the PRN code, $\bar{\tau}$ is the candidate code phase, and \bar{f}_D is the candidate Doppler shift (or more in general the candidate frequency offset). According to the Maximum Likelihood (ML) estimation, the estimates of the Doppler shift \hat{f}_D and of the code shift $\hat{\tau}$ can be found as:

$$(\hat{f}_D, \hat{\tau}) = \arg \max_{(f_D, \bar{\tau})} \left| \frac{1}{N} \sum_{n=0}^{N-1} y_{IF}[n] r_{IF}^*[n - \bar{\tau}] \right|^2 \quad (6)$$

The dimensions of the search space depend on the specific scenario, including the range of possible Doppler shift values and the length of the code being processed. Consequently, employing a parallel FFT-based acquisition scheme is strongly recommended to efficiently handle the computational complexity. In this case the CAF can be obtained as:

$$S(\bar{\tau}, \bar{f}_D) = \Re(Y(\bar{\tau}, \bar{f}_D) \cdot Y(\bar{\tau}, \bar{f}_D)^*) \quad (7)$$

where:

$$Y(\bar{\tau}, \bar{f}_D) = \frac{1}{N} \text{IDFT}\{\text{DFT}(y_{IF}) \cdot \text{DFT}(r_{IF})^*\} \quad (8)$$

The extension of the coherent integration time, which involves performing correlation over multiple periods of the PRN code, ideally increases the sensitivity of the receiver's acquisition stage. However, in some cases, the GNSS signal may be modulated by a data bit component, which limits the coherent integration time due to the transitions of the data bits.

The non-coherent integration allows to overcome this issues by performing separately the correlation over consecutive and non overlapping time windows, and then non-coherently accumulating them. The equation for non-coherent integration,

which accumulates the squared magnitude of the CAF over multiple non-overlapping time windows, can be expressed as:

$$S_{NC}(\bar{\tau}, \bar{f}_D) = \sum_{k=1}^K \left| \frac{1}{N} \sum_{n=0}^{N-1} y_{IF}^{(k)}[n] r_{IF}^{(k)*}[n - \bar{\tau}] \right|^2 \quad (9)$$

where:

- $S_{NC}(\bar{\tau}, \bar{f}_D)$ is the non-coherent accumulation of the CAF.
- K is the number of non-coherent sums.
- $y_{IF}^{(k)}[n]$ is the received signal in the k -th time window.
- $r_{IF}^{(k)}[n]$ is the local code replica for the k -th time window, which includes the candidate Doppler shift \bar{f}_D .
- $\bar{\tau}$ is the candidate code phase.
- \bar{f}_D is the candidate Doppler shift.

1) Doppler shift compensation on the local code replica:

As reported in the literature [11] [2], the presence of Doppler on the received code can degrade performance during the acquisition stage, leading to reduced receiver sensitivity, particularly when longer coherent integration times and significant Doppler shifts on the carrier are involved. Moreover, uncompensated Doppler on the code induces a shift in the estimated code delay during acquisition. The effect of Doppler on the spreading code can be interpreted as a stretch or contraction of the timescale, resulting in a different code rate, as denoted in the expression (3). The chip rate R_D of a signal affected by Doppler shift can be expressed as:

$$R_D = R_{\text{chip}} \left(1 + \frac{f_D}{f_{\text{carrier}}} \right) \quad (10)$$

Adapting the local code replica chip rate to the candidate Doppler shift should allow to minimize the loss due to the effect of the Doppler shift on the received signal code, as reported in [11]. To compensate for the effects of Doppler shift on the PRN code, a local code replica can be generated with a modified chip rate R_D . The length of the generated replica should align with the duration of the signal segment accumulated, whether using the coherent or non-coherent approach. This ensures that the code remains synchronized over time with that of the received signal.

2) *Exhaustive data bit search:* When dealing with a signal modulated by a data bit channel, the extension of the coherent integration time is constrained by the occurrence of bit transitions. These transitions can reduce or entirely negate the benefits of the extended coherent integration time [12]. In contrast, the non-coherent integration process is less sensitive to such transitions; however, the introduction of squaring loss [13] introduces certain performance limitations. Usually, the coherent integration time can be extended considering the pilot component of the GNSS signal broadcasted, but this is not the case of the GPS Coarse/Acquisition (C/A) signal, since this signal does not include a pilot component. To enable the extension of coherent integration time without resorting to non-coherent approaches, this work presents an optimized technique, initially proposed in [14], that compensates for phase transitions induced by unknown data bits modulating

the received GPS C/A (G1C) signals. To account for data bit transitions, an exhaustive search of all potential transition sequences within the portion of the received signal under analysis would typically be required. The test can be conducted by multiplying the local code replica with the bit sequence under test, and then evaluating the CAF over the entire selected Doppler-delay search space. The sequence leading to the maximum value of the CAF can be considered the best estimate of the data bit component.

However, leveraging the properties of the transmitted signal and the circular FFT-based correlator, certain optimizations can be introduced.

As shown in [14], one key optimization arises from the fact that bit transitions are always aligned with the start of the PRN code epochs. This alignment constrains the set of possible phase shifts in the bit transition sequence to be considered. Consequently, since the data bit rate is typically an integer multiple of the inverse of the primary code length, the analysis can be simplified by multiplying the local code replica with the bit sequence under evaluation, aligning the bits with the start of the local code replica. Given an input signal of length $L = N_b \cdot L_{\text{bit}}$, where $N_b \in \mathbb{Z}$ and L_{bit} represents the length of a single bit, the number of the data bit to be found is $N_b + 1$. By appending an additional bit to the bit sequence under test, and extending the received signal with a zero-padding of length L_{bit} , it is possible to compensate for all uncompensated bit transitions at both the beginning and the end of the received signal.

This approach ensures that the correlation analysis accounts for potential misalignment caused by transitions at the signal boundaries. The obtained set of bit sequences to be tested is :

$$\mathcal{B}_{\text{TOT}}^{N_b+1} = \{\mathbf{b}_i \mid \mathbf{b}_i \in \{-1, 1\}^{N_b+1}, i \in \{1, \dots, 2^{N_b+1}\}\} \quad (11)$$

However, considering the CAF in (4) and in (7), it is shown that the correlation function is squared. This implies that if the local code replica is multiplied by a bit sequence of opposite sign to that of the received signal, the resulting negative correlation is also squared. Consequently, it becomes indistinguishable from the correlation obtained when the local bit sequence has the same sign as that of the received signal. This implies that the set of possible bit sequences to be tested can be halved. For example, the bit sequence $[-1, 1, -1, -1]$ results in the same CAF obtained by considering the sequence $[1, -1, 1, 1]$, so it is necessary to test for only one of the two mentioned bit sequences. The resulting set of bit sequences is:

$$\mathcal{B}_h^{N_b+1} = \{\mathbf{b}_i \mid \mathbf{b}_i \in \{-1, 1\}^{N_b+1}, i \in \{1, \dots, 2^{N_b}\}\} \quad (12)$$

Additionally, another optimization can be employed to further reduce the computational complexity of the exhaustive bit search. The FFT-based correlator described in (8) operates as a circular correlator, meaning that code shifts $\bar{\tau}$ are evaluated by circularly shifting one input signal relative to the other.

As a result, it can be observed that the set of bit sequences to be tested contains redundancies. For instance, the bit sequence $[-1, 1, -1, -1]$ is equivalent to the circularly shifted versions

of $[1, -1, -1, -1]$, $[-1, -1, 1, -1]$, and $[-1, -1, -1, 1]$. Since this step of the processing chain is not concerned with demodulating the navigation message, testing only one representative sequence from each equivalence class of circularly shifted sequences is sufficient. This approach further reduces the computational burden.

In the context of combinatorics, an a -ary necklace of length l is a sequence of l elements, where each element can be one of a possible types. Rotational symmetry is considered, meaning that two strings $b_1 b_2 \dots b_l$ and $b_k b_{k+1} \dots b_l b_1 b_2 \dots b_{k-1}$ are regarded as equivalent for any k . In the case of this study, the necklace considered is binary and has a length of $l = N_b + 1$. As reported in the literature [15] [16], the number of distinct fixed necklaces of length l composed of a types of beads, denoted as $N_{nl}(l, a)$, is given by:

$$N_{nl}(l, a) = \frac{1}{l} \sum_{i=1}^{\nu(l)} \phi(d_i) a^{l/d_i} \quad (13)$$

where:

- d_i are the divisors of l .
- $\nu(l)$ is the number of divisors of l .
- $\phi(x)$ is the totient function [17].

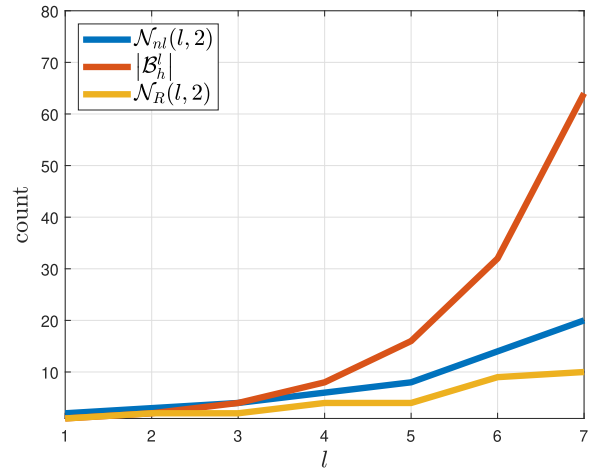


Fig. 2: Comparison between the cardinality of the set \mathcal{B}_h^l , the number of unique binary necklaces $N_{nl}(N_b + 1, 2)$, and the cardinality of sign-blind binary necklaces $N_R(N_b + 1, 2)$ as a function of l .

Exploiting the set of $N_{nl}(N_b + 1, 2)$ necklaces, it is possible to reduce the number of binary sequences to be tested. However, considering the sign-blindness of the CAF, the number of sequences can be further reduced. Thus, the set of necklaces to be tested can be expressed as $N_R(N_b + 1, 2)$. In Fig. 2 are reported the different number of sequences as a function of l . The set of sequences under test can then be expressed as:

$$\mathcal{B}_{\mathcal{R}} = \{b_1, \dots, b_{N_R(N_b+1,2)}\}. \quad (14)$$

Given that all bit sequences under test must be evaluated across the entire Doppler-delay search space, leveraging sign-blind

necklaces allows for a reduction in the total search space compared to the scenario where all bit sequences in $B_{\text{TOT}}^{N_b+1}$ are tested. After having tested all the sequences in $\mathcal{B}_{\mathcal{R}}$, by multiplying them for the local code replica, for all the bins of the Doppler-delay search space, the values of $\bar{\tau}$ and \bar{f}_D leading to the maximum value of CAF are then selected as estimates of the delay τ and of the Doppler shift f_D . As demonstrated in [7], it is not possible to derive an analytical expression for the false alarm and detection probabilities in the case of exhaustive bit search. Therefore, in this work, the method used to declare successful acquisition is based on the measurement of the peak-to-noise-floor standard deviation ratio, and testing it against a given threshold. This metric was chosen for its simplicity. However, acquisitions flagged as successful are further verified by re-testing with longer integration times and performing the acquisition over different non-overlapping time windows. If acquisition is successful in all cases, it is deemed definitive. Given that the nature of this test differs from the standard and well-defined ML approach, the results obtained using the bit search method are analyzed separately from those obtained with more conventional approaches in the following sections, with the former explicitly flagged.

B. Simulation Framework

In this study, a hardware-in-the-loop setup is employed to generate realistic signal sample batches that can be post-processed. The experimental setup in Qascom Srl premises consists of three elements:

- A Spirent GSS7000 Radio-Frequency Constellation Simulator (RFCS) signal generator to simulate the real mission operations signals.
- A Low-Noise Amplifier (LNA) specifically designed in the LuGRE mission framework to isolate the receiving signals from noise and interferences.
- The LuGRE payload GNSS receiver developed by Qascom that collects the signal sample batches during the simulation.

The theoretical LuGRE payload performance in space has been simulated in a synthetic environment, emulating the mission scenarios of interest. Several points in the Moon Transfer Orbit (MTO) trajectories have been selected, as well as in Low Lunar Orbit (LLO) and in Moon Surface (MS). Specifically, the scenarios considered in this paper include distances of 14 Radii Earth (RE) from the Earth, as well as 30, 45, 54, and 60 RE, and the Moon Surface (this scenario is labeled in the following sections as MS).

Several analyses [18] have been conducted on the GNSS signals power, to create Spirent scenarios matching what is expected during real operations in the best possible way.

IV. EXPERIMENTAL RESULTS

The dataset acquired using the experimental setup described in Section III-B is processed using the techniques outlined in Section III-A. Table II provides a summary of the acquired PRNs, including the techniques employed and the corresponding parameter selections. For each operation window and

individual signal, an overview of the simulated scenario is presented. Specifically, the tracking status of each spreading code during the Real-Time Processing (RTP) phase is detailed, indicating whether it was initially tracked at t_0 or acquired later at a specific time t . Additionally, for signals that are successfully tracked during the RTP phase, Table II includes the first available estimates of the C/N_0 at the tracking stage. Furthermore, Table II also indicates whether Doppler compensation on the code was necessary to achieve successful acquisition for each configuration. Each configuration was tested both with and without compensation; if both attempts were unsuccessful, alternative configurations were evaluated. The table also reports the minimum required dwell time T_s that enabled successful acquisition, among the configurations presented in Table III. All acquisitions are conducted both with and without Doppler compensation, except in instances where bit search is performed, in which case Doppler compensation is always enabled. In such cases, the acquisition is deemed successful, as outlined in Section III-A, based on a peak-to-noise-floor standard deviation threshold of 20, considering the coherent integration time of 160 *ms*. In the following sections IV-A and IV-B a more detailed analysis of the results is carried on, in particular IV-A focuses on reporting the results obtained limiting the complexity and the signal length required at the acquisition stage, while section IV-B focuses on the results obtained with longer integration times.

A. Limited complexity and dwell time

A series of acquisitions is performed using a non-coherent integration technique. To ensure a consistent comparison across all operational windows considered, a fixed combination of non-coherent sums and coherent integration time is selected for each signal in this analysis. For GPS C/A (G1C), the chosen parameters are $k = 10$ and $T_{\text{coh}} = 8$ ms, while for Galileo E1C, the parameters are $K = 1$ and $T_{\text{coh}} = 100$ ms.

It is important to note that the parameters of the two signals differ, as the Galileo E1C signal includes a pilot component, whereas the GPS C/A (G1C) signal does not.

The size of the Doppler bins is chosen based on the coherent integration time, adhering to the empirical rule that the Doppler bin width Δf_D should be less than $\frac{2}{3T_{\text{coh}}}$, where T_{coh} represents the coherent integration time. In particular in this section Δf_D for the G1C is 10 *Hz*, while for the E1C case is 2 *Hz*. The technique introduced in section III-A for the compensation of the Doppler effect on the code is compared with a standard coherent/non-coherent integration. This comparison allows for a better understanding of the necessity of utilizing the Doppler compensation technique and evaluating its performance in the described scenario.

Fig. 3 presents a comparison of estimated C/N_0 values obtained through acquisitions of the G1C signal, with Doppler shift correction (denoted by a round marker), and those obtained via standard non-coherent acquisition (denoted with a diamond marker). Similarly, Fig. 4 presents the same type of measurement as in Fig. 3, but for the Galileo E1C signal. The available data density in Fig. 3 limits the ability to identify

WIN	Signal	PRN	Tracked @ t_s	Tracked @ t [s]	Tracking C/N_0 [dBHz]	Min T _d [ms]	K	T _{coh} [ms]	Dopp. Comp.	Bit search	
14RE	G1C	21	Y	0	42	24	6	4	N	-	
		7	N	60	37	24	6	4	N	-	
		16	N	60	34	24	6	4	N	-	
		26	N	60	31	24	6	4	N	-	
		27	N	N	-	24	6	4	Y	-	
		4	N	120	33	80	10	8	N	-	
		3	N	60	28	120	1	120	Y	Y	
		17	N	480	27	140	1	140	Y	Y	
	8	N	330	24	140	1	140	Y	Y		
	E1C	10	Y	0	37	100	1	100	N	-	
		5	Y	0	34	100	1	100	N	-	
		36	Y	0	32	100	1	100	Y	-	
		12	Y	0	30	100	1	100	N	-	
		9	N	60	32	200	1	200	Y	-	
		31	Y	0	30	400	2	200	Y	-	
		9	Y	0	33	400	2	200	Y	-	
		4	N	150	25	400	2	200	Y	-	
		L5Q	26	N	150	35	30	30	1	N	-
			8	N	332	32	30	30	1	Y	-
	E5aI	10	N	60	38	15	15	1	N	-	
		12	N	60	32	30	30	1	N	-	
		5	N	120	36	30	30	1	Y	-	
		36	N	120	33	30	30	1	Y	-	
	30RE	G1C	27	N	180	30	24	6	4	N	-
16			N	180	30	24	6	4	Y	-	
7			N	180	31	24	6	4	Y	-	
26			N	N	-	120	1	120	Y	Y	
E1C		10	Y	0	42	100	1	100	N	-	
		4	N	180	24	600	2	300	Y	-	
31		N	N	-	300	2	600	Y	-		
L5Q		26	N	N	-	30	30	1	Y	-	
E5aI	10	N	25	38	15	15	1	N	-		
45RE	G1C	27	N	180	30	24	6	4	Y	-	
		16	N	180	28	24	6	4	Y	-	
		7	N	250	28	80	10	8	N	-	
	E1C	11	Y	0	35	100	1	100	N	-	
		24	N	180	29	100	1	100	N	-	
	E5aI	11	N	60	37	30	30	1	Y	-	
54RE	G1C	1	N	180	33	24	6	4	N	-	
	3	N	N	-	140	1	140	Y	Y		
	E1C	11	Y	0	35	100	1	100	N	-	
	L5Q	1	N	210	39	15	15	1	N	-	
E5aI	11	N	60	37	15	15	1	N	-		
60RE	G1C	16	Y	0	41	24	6	4	N	-	
	10	Y	0	39	24	6	4	N	-		
	E1C	12	N	300	26	100	1	100	Y	-	
L5Q	10	Y	0	43	15	15	1	N	-		
MS	G1C	2	Y	0	42	24	6	4	N	-	
		29	Y	0	31	80	10	8	N	-	
		20	N	60	27	80	10	8	Y	-	
		24	N	224	26	80	10	8	N	-	
	L5Q	24	N	202	29	15	15	1	N	-	

TABLE II: Results of the acquisition test campaign, along with the parameters selected for the acquisition, the technique used, and the minimum dwell time, based on the parameter set described in Table III.

a general trend in the C/N_0 of the acquired satellites for each acquisition technique as a function of altitude, due to the sparse distribution of data points. This consideration holds also for the Galileo E1C case. From Figs. 3 and 4, it can be observed that the C/N_0 estimates obtained after compensating for the Doppler shift effects on the PRN codes appear to be higher than those obtained without this correction. This behavior may be justified by the fact that when the effect of the Doppler on the PRN code are not compensated the correlation peak is deteriorated, introducing a loss in the estimated C/N_0 . In some cases, given the selected acquisition parameters, the

Signal	T _s [ms]	K	T _c [ms]	Bitsearch
G1C	24	6	4	N
	80	10	8	N
	100	1	100	Y
	120	1	120	Y
E1C	140	1	140	Y
	100	1	100	N
	200	1	200	N
	400	2	200	N
E5aI	600	3	200	N
	15	1	15	N
L5Q	30	1	30	N
	15	15	1	N
	30	30	1	N
	60	30	2	N

TABLE III: Acquisition parameters.

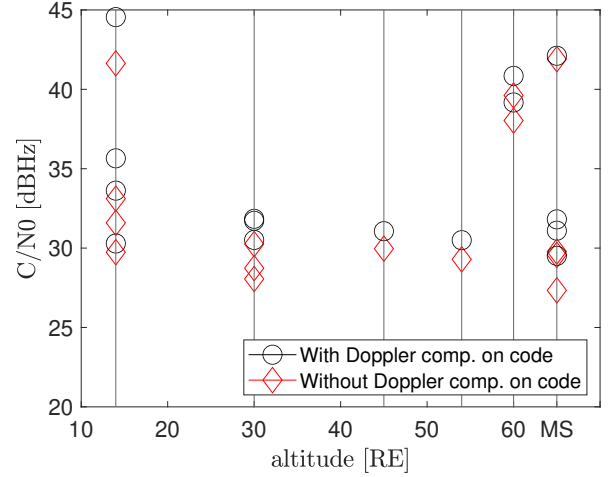


Fig. 3: Comparison between the C/N_0 estimated with and without the Doppler compensation on the local code replica as a function of the altitude. The acquisition parameters are $K = 10$, $T_c = 8$ ms, $P_{FA} = 0.001$. The bit removal is not employed. Signal: G1C.

acquisition is successful only when Doppler compensation on the local code replica is performed. In these cases, only the corresponding round marker is reported. The gain of Doppler compensation on the code, relative to standard coherent/non-coherent techniques, is evaluated as the difference in C/N_0 with and without compensation, using the same acquisition parameters of Figs. 3 and 4. Subsequently, the distribution of all the differences for all the operation windows is then reported in Fig. 5.

Fig. 6 presents the estimated C/N_0 values obtained from processing the E5aI signal. The acquisition parameters used are $K = 30$, $T_c = 1$ ms, and $P_{FA} = 0.001$. As shown in the figure, Doppler compensation on the code generally results in higher C/N_0 estimates. The resulting gains are depicted in Fig. 7.

To summarize the results, Fig. 8 illustrates the relationship between the Doppler shift and the gain achieved by compensating for the Doppler shift on the code. The acquisition parameters considered are consistent with those used in the

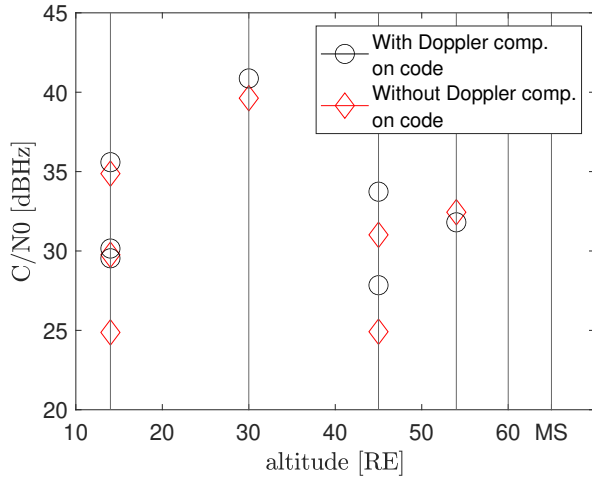


Fig. 4: Comparison between the C/N_0 estimated with and without the Doppler compensation on the local code replica as a function of the altitude. The acquisition parameters are $K = 1$, $T_c = 100 \text{ ms}$, $P_{FA} = 0.001$. Signal: Galileo E1C.

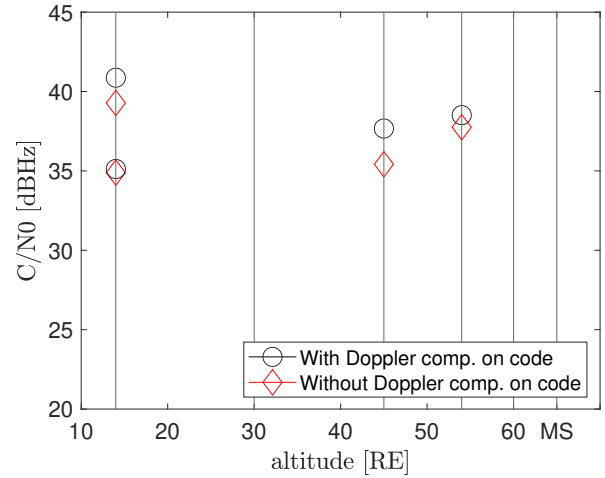


Fig. 6: Comparison between the C/N_0 estimated with and without the Doppler compensation on the local code replica as a function of the altitude. The acquisition parameters are $K = 30$, $T_c = 1 \text{ ms}$, $P_{FA} = 0.001$. Signal: E5aI.

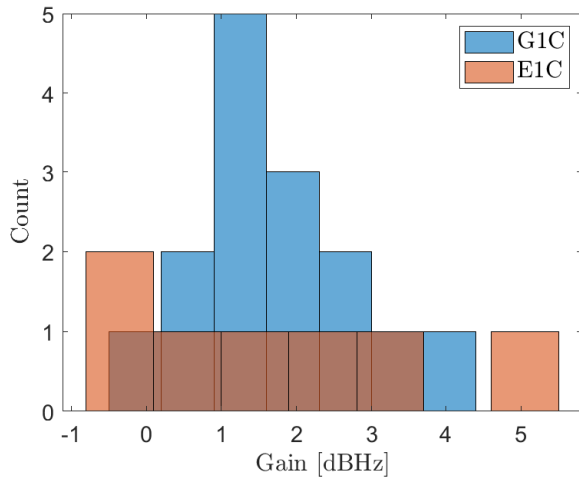


Fig. 5: Distribution of the gain obtained compensating for the Doppler shift on the local code replica. Signals: G1C, E1C.

scenarios presented in Figs. 3, 4, and 7. Fig. 8 (bottom) shows the distribution of successful acquisitions, $N_{D,\text{only}}$, achieved exclusively through Doppler compensation on the code. As it is possible to notice from Fig. 8 the gain of the C/N_0 seems to be correlated with the Doppler, larger Doppler shifts induces larger losses on the C/N_0 . The gain is calculated only for successful acquisitions, both with and without code Doppler compensation. Notably, compensation proves essential for acquisition in scenarios where it would otherwise fail, as illustrated in the lower section of Fig. 8.

B. Acquisition with longer coherent integration times.

This section, which focuses on the analysis of L1/E1 signals, presents the results of a series of acquisitions performed using

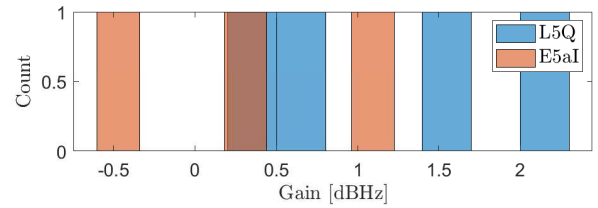


Fig. 7: Distribution of the gain obtained compensating for the Doppler effect on the local code replica. The acquisition parameters are $K = 30$, $T_c = 1 \text{ ms}$, $P_{FA} = 0.001$.

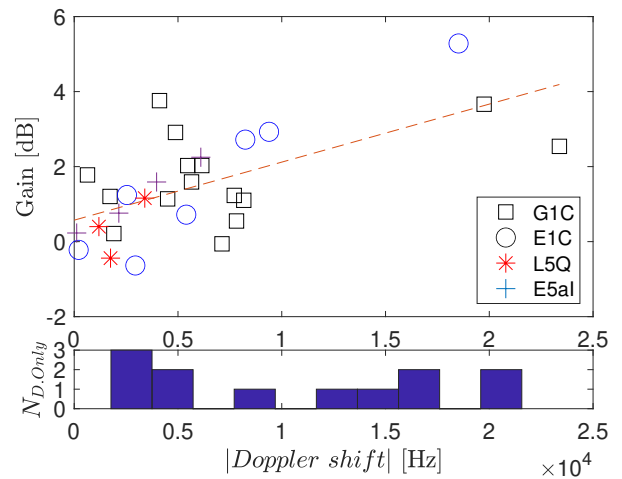


Fig. 8: Gain vs. Doppler shift (top) and distribution of successful acquisitions achieved exclusively through Doppler compensation on the code (bottom).

extended segments of the available signals. For what concerns GPS C/A, it is chosen to perform a data bit search considering different coherent integration times T_{coh} , spanning from 100 ms up to 160 ms. In the following Figures are reported the results obtained considering the operation window at 14, 30 and 54 RE. Fig. 9 through 11 illustrate the improvement in

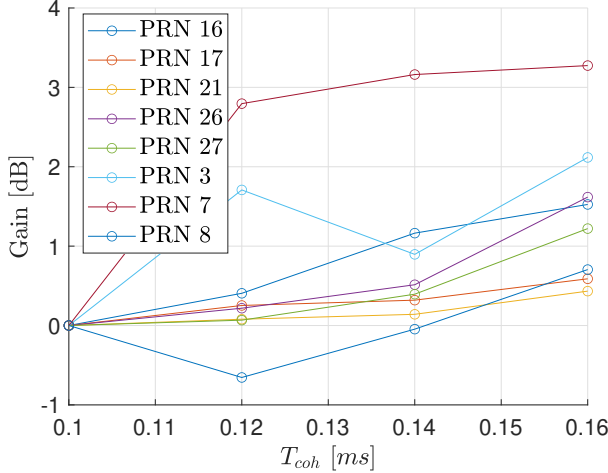


Fig. 9: Improvement in the peak-to-noise floor ratio relative to the peak-to-noise ratio achieved with a 100 ms coherent integration time, expressed as a function of the coherent integration time T_{coh} . Signal: G1C, Method: Bit search, Operation window: 14 RE.

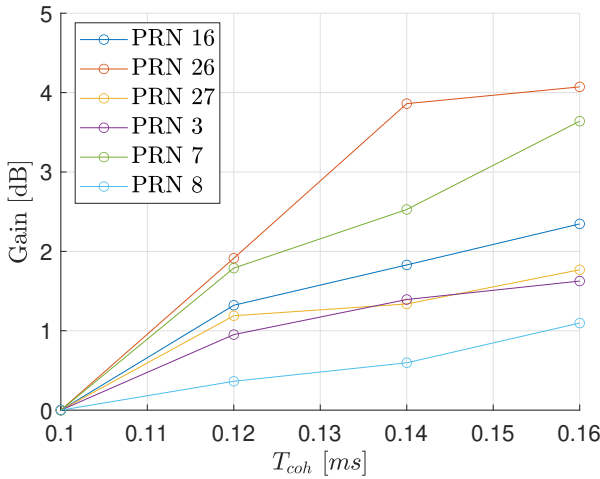


Fig. 10: Improvement in the peak-to-noise floor ratio relative to the peak-to-noise ratio achieved with a 100 ms coherent integration time, expressed as a function of the coherent integration time T_{coh} . Signal: G1C, Method: Bit search, Operation window: 30 RE.

the peak-to-noise floor ratio relative to the peak-to-noise ratio achieved with a 100 ms coherent integration time, expressed as a function of the coherent integration time T_{coh} . As observed, increasing the coherent integration time generally leads to an

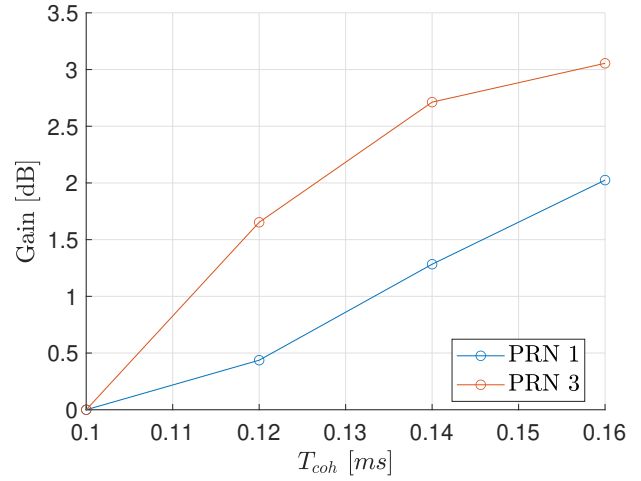
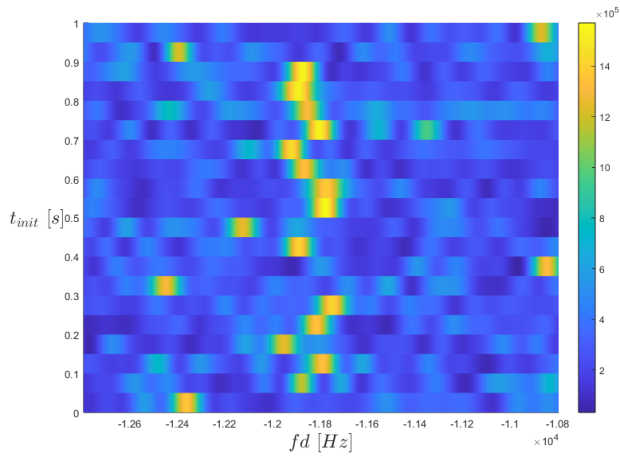


Fig. 11: Improvement in the peak-to-noise floor ratio relative to the peak-to-noise ratio achieved with a 100 ms coherent integration time, expressed as a function of the coherent integration time T_{coh} . Signal: G1C, Method: Bit search, Operation window: 54 RE.

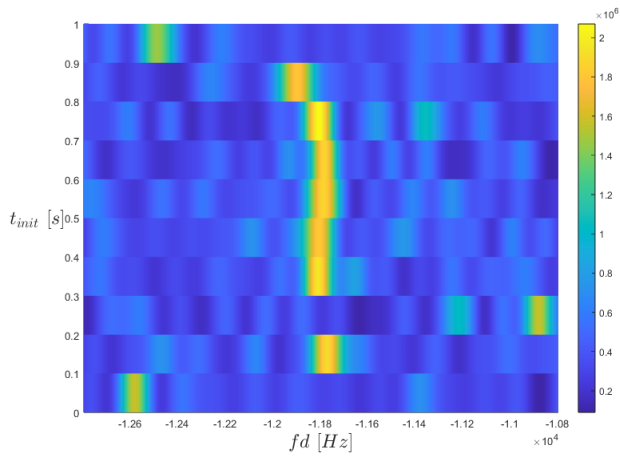
improvement in the peak-to-noise floor ratio. However, in Fig. 9, the increase in the ratio appears less pronounced in some cases.

The data bit search enhances the correlation peak of acquired signals and increases the number of visible PRNs, as shown in Table II.

Processing longer segments of the signal could provide deeper insights into the behavior of the correlation peak over time. By performing acquisitions over distinct time windows within the input signal and comparing the resulting CAF in either the delay or Doppler shift domain, it becomes possible to better analyze the signal's characteristics and assess its persistence over time. The estimation of the Doppler shift or code phase corresponding to the peak of the CAF, obtained by processing different time windows of the signal separated by a few tens of milliseconds, may be subject to noise. This is particularly evident when the coherent integration time for each acquisition is short relative to the C/N_0 . However, analyzing and comparing the results from each acquisition over time can yield valuable insights. In the following are presented the results obtained by processing the signal within the operational window at 14 RE, focusing specifically on PRN 3 and the G1C signal. The CAF was computed for a signal segment starting at time t_{init} . Fig. 12a and Fig. 12b show slices of the CAF in the Doppler shift domain, corresponding to the peak of the CAF as a function of t_{init} , for two different parameter sets selected during the acquisition stage. Specifically, Fig. 12a presents the results obtained with $K = 5$ and $T_{coh} = 8$ ms, while Fig. 12b illustrates the results for $K = 7$ and $T_{coh} = 8$ ms. The signal segments corresponding to each t_{init} are non-overlapping.



(a) $K = 5$ and $T_{coh} = 8$ ms



(b) $K = 7$ and $T_{coh} = 8$ ms

Fig. 12: Multiple, subsequent CAFs obtained by testing 1 s signal batch.

V. CONCLUSION

Experimental results confirm that compensating for Doppler-induced distortions on the PRN code leads to significant improvements in acquisition sensitivity. Specifically, the peak-to-noise-floor ratio exhibits an average gain of 2–3 dB, with some cases achieving up to 5 dB improvement. Additionally, the Doppler-compensated approach enables the acquisition of satellites that would otherwise remain undetected, increasing the number of successfully acquired PRNs by 30%–50% across different operational windows. The exhaustive bit search technique further enhances acquisition robustness, allowing for coherent integration times up to 160 ms, which improves detection sensitivity by an additional 3 dB compared to standard non-coherent approaches. These findings establish a baseline for evaluating high-sensitivity acquisition techniques on actual mission data once publicly released to the GNSS community. The demonstrated improvements reinforce the feasibility of GNSS-based Positioning, Navigation, and

Timing (PNT) in cislunar space, providing critical insights for future lunar and deep-space exploration missions.

ACKNOWLEDGEMENT

This study was funded within the contract n. 2021-26-HH.0 between Agenzia Spaziale Italiana and Politecnico di Torino "Attività di Ricerca e Sviluppo inerente alla Navigazione GNSS nello Space volume Terra/Luna nell'ambito del Lunar GNSS Receiver Experiment". This publication is also part of the project PNRR-NGEU which has received funding from the MUR – DM 630/2024.

REFERENCES

- [1] L. Konitzer, J. J. Parker, B. Ashman, N. Esantsi, C. Facchinetti, F. Dovis, A. Minetto, A. Nardin, F. Bauer, L. Ansalone *et al.*, "Science objectives and investigations for the lunar GNSS receiver experiment (LuGRE)," in *Proceedings of the 37th International Technical Meeting of the Satellite Division of The Institute of Navigation (ION GNSS+ 2024)*, 2024, pp. 1061–1081.
- [2] A. Nardin, A. Minetto, O. Vouch, M. Mariani, and F. Dovis, "Snapshot acquisition of GNSS signals in space: a case study at lunar distances," in *Proceedings of the 35th International Technical Meeting of the Satellite Division of The Institute of Navigation (ION GNSS+ 2022)*, 2022, pp. 3603–3617.
- [3] A. Nardin, A. Minetto, S. Guzzi, F. Dovis, L. Konitzer, and J. J. Parker, "Snapshot tracking of GNSS signals in space: A case study at lunar distances," in *Proceedings of the 36th International Technical Meeting of the Satellite Division of The Institute of Navigation (ION GNSS+ 2023)*, 2023, pp. 3267–3281.
- [4] P. F. Silva, H. D. Lopes, T. Peres, J. Silva, J. Ospina, F. Cichocki, F. Dovis, L. Musumeci, D. Serant, T. Calmettes *et al.*, "Weak GNSS signal navigation to the moon," in *Proceedings of the 26th International Technical Meeting of the Satellite Division of The Institute of Navigation (ION GNSS+ 2013)*, 2013, pp. 3357–3367.
- [5] H. D. Lopes, J. S. Silva, P. F. Silva, L. Musumeci, F. Dovis, D. Serant, T. Calmettes, R. Challamel, J. A. Ospina, I. Pessina *et al.*, "GNSS-based navigation for lunar missions," in *Proceedings of the 27th International Technical Meeting of the Satellite Division of The Institute of Navigation (ION GNSS+ 2014)*, 2014, pp. 1536–1553.
- [6] J. J. Parker, F. Dovis, B. Anderson, L. Ansalone, B. Ashman, F. H. Bauer, G. D'amore, C. Facchinetti, S. Fantinato, G. Impresario *et al.*, "The lunar GNSS receiver experiment (LuGRE)," in *Proceedings of the 2022 International Technical Meeting of The Institute of Navigation*, 2022, pp. 420–437.
- [7] D. Borio, "A statistical theory for GNSS signal acquisition," PhD thesis, Politecnico di Torino, 2008.
- [8] D. Gómez Casco, "Non-coherent acquisition techniques for high-sensitivity GNSS receivers," Ph.D. dissertation, Universitat Autònoma de Barcelona, 2018.
- [9] M. Villanti, P. Salmi, and G. E. Corazza, "Differential post detection integration techniques for robust code acquisition," *IEEE transactions on communications*, vol. 55, no. 11, pp. 2172–2184, 2007.
- [10] F. Dovis and T. H. Ta, "High sensitivity techniques for GNSS signal acquisition," in *Global navigation satellite systems: Signal, theory and applications*. InTech, 2012, pp. 3–32.
- [11] M. Focreas, O. Julien, C. Macabiau, and B. Ekambi, "Detailed analysis of the impact of the code Doppler on the acquisition performance of new GNSS signals," in *Proceedings of the 2014 International Technical Meeting of The Institute of Navigation*, 2014, pp. 513–524.
- [12] D. Borio, M. Fantino, and L. L. Presti, "The impact of the Galileo signal in space in the acquisition system," in *Satellite Communications and Navigation Systems*. Springer, 2008, pp. 151–167.
- [13] C. Strassle, D. Megnet, H. Mathis, and C. Burgi, "The squaring-loss paradox," in *Proceedings of the 20th International Technical Meeting of the Satellite Division of The Institute of Navigation (ION GNSS 2007)*, 2007, pp. 2715–2722.
- [14] L. Sciacca, "Advanced signal processing techniques for GNSS signals quality analysis," Master's thesis, Politecnico di Torino, 2024.
- [15] F. Ruskey and J. Sawada, "An efficient algorithm for generating necklaces with fixed density," *SIAM Journal on Computing*, vol. 29, no. 2, pp. 671–684, 1999.

- [16] H. Fredricksen and I. J. Kessler, "An algorithm for generating necklaces of beads in two colors," *Discrete mathematics*, vol. 61, no. 2-3, pp. 181–188, 1986.
- [17] D. Lehmer, "On Euler's totient function," *Bulletin of the American Mathematical Society*, vol. 38, pp. 745–751, 1932.
- [18] S. Tedesco, F. Bernardi, S. Guzzi, M. Boschiero, M. Pulliero, D. Marcantonio, M. Ghedin, E. Miotti, S. Fantinato, O. Pozzobon *et al.*, "Deep space GNSS in moon transfer orbit: the LuGRE receiver," in *2023 IEEE International Conference on Wireless for Space and Extreme Environments (WiSEE)*. IEEE, 2023, pp. 1–6.